Accepted Manuscript

Broad first-order magnetic entropy change curve in directionally solidified polycrystalline Ni-Co-Mn-In

F. Chen, Y.X. Tong, L. Li, J.L. Sánchez Llamazares, C.F. Sánchez-Valdés, P. Müllner

PII: S0925-8388(17)32847-5

DOI: 10.1016/j.jallcom.2017.08.118

Reference: JALCOM 42875

To appear in: *Journal of Alloys and Compounds*

Received Date: 13 March 2017

Revised Date: 24 July 2017

Accepted Date: 13 August 2017

Please cite this article as: F. Chen, Y.X. Tong, L. Li, J.L. Sánchez Llamazares, C.F. Sánchez-Valdés, P. Müllner, Broad first-order magnetic entropy change curve in directionally solidified polycrystalline Ni-Co-Mn-In, *Journal of Alloys and Compounds* (2017), doi: 10.1016/j.jallcom.2017.08.118.

Author agreement

On behalf all authors, I will guarantee the following aspects :

(1) All authors have participated sufficiently in this work to take public responsibility for it;

(2) All authors have reviewed the final version of the manuscript and approve it for publication;

(3) Neither this manuscript nor one with substantially similar content under our authorship has been published or is being considered for publication elsewhere.

Broad first-order magnetic entropy change curve in directionally solidified polycrystalline Ni-Co-Mn-In

F. Chen[1,*], Y.X Tong [1], L. Li[1], J. L. Sánchez Llamazares[2,*], C. F. Sánchez-Valdés[3], P. Müllner [4]

[1] Institute of Materials Processing and Intelligent Manufacturing, College of Materials Science and Chemical Engineering, Harbin Engineering University, Harbin, 150001, China.
[2] Instituto Potosino de Investigación Científica y Tecnológica A.C., Camino a la Presa San José 2055, Col. Lomas 4ª sección, San Luis Potosí, S.L.P. 78216, México
[3] División Multidisciplinaria, Ciudad Universitaria, Universidad Autónoma de Ciudad Juárez (UACJ), calle José de Jesús Macías Delgado # 18100, Ciudad Juárez, Chihuahua, México
[4] Micron School of Materials Science and Engineering, Boise State University, ID 83725, US

[*] Corresponding author:
Dr. Feng Chen
Institute of Materials Processing and Intelligent Manufacturing
College of Materials Science and Chemical Engineering
Harbin Engineering University
No.145 Nan Tong Street, Nan-Gang District
Harbin 150001, CHINA
Tel: +86-0451-82518173
E-mail address: chenfeng01@hrbeu.edu.cn

[*] Corresponding author:
Dr. José Luis Sánchez Llamazares
Instituto Potosino de Investigación Científica y Tecnológica A.C.,
Camino a la Presa San José 2055, Col. Lomas 4ª sección,
San Luis Potosí, S.L.P. 78216, México
Tel: +52-444-8342000
E-mail address: jose.sanchez@ipicyt.edu.mx

Abstract

We present the thermal dependence of the magnetic entropy change $\Delta S_M(T)$ across the martensitic transformation for a polycrystalline sample, which was cut from a directionally solidified rod, with a nominal composition $Ni_{42}Co_8Mn_{38}In_{12}$ grown by the Bridgman-Stockbarger technique. This material combines a first-order martensitic transformation expanded over a very large working temperature range with a large magnetization change of ~86 A m^2 kg^{-1}. Accordingly, for a magnetic field change of 5 T (2 T), the coupled magneto-structural transition gives rise to a broad magnetic entropy change curve across the reverse martensitic transformation with a moderate maximum value of 6.8 (3.0) J kg^{-1} K^{-1} and a full-width at half-maximum δT_{FWHM} for the $\Delta S_M(T)$ curve of 49 (43) K. Such a broad structural transition may be due to the effect of chemical segregation introduced by the directional solidification which can be enhanced by the non-uniform distribution of second phase particles. Accompanying with such a wide working temperature range, a large refrigerant capacity of 334 J kg^{-1} was obtained for a field change of 5 T.

Keywords: Ni-Co-Mn-In; ferromagnetic shape memory alloy; broad martensitic transformation; magnetocaloric properties; working temperature range.

I. INTRODUCTION

The off-stoichiometric Ni-Mn-Z Heusler alloys, with Z = In, Sb and Sn, have become an important group of promising magnetic refrigerants due to their tunable temperature and giant magnetic-field induced magnetocaloric effect (MCE) associated to the first-order diffusionless martensitic transformation [1-6]. In these materials small compositional changes, or the addition of a four substitutional element, allow the tuning of the structural transition temperatures over a wide temperature range from low to room temperature (RT) or even above [7-13]. As the following examples show, for Ni-Mn-Z Heusler alloys, structural transition temperatures are highly sensitive to the chemical composition. In $Ni_{50}Mn_{37+x}Sb_{13-x}$ (x = 0.0, 0.5, 1.0) alloys, martensitic transformation temperature can be set between 275 and 300 K through a slight variation in the content of Mn and Sb [8]. For $Ni_{50-x}Mn_{39+x}Sn_{11}$ (x = 5, 6, 7) alloys, martensitic transformation start temperature (M_s) gradually drops from 270 K to 245 K, and then down to 200 K with increasing Mn concentration [9]. For Co-containing $Ni_{44-x}Co_xMn_{45}Sn_{11}$ (x = 0, 1, 2) alloys, martensitic reverse transformation start temperature, A_s decreases by 56 K from 245 to 189 K by addition of 2 at. % Co [11]. Only a small addition of Fe (x = 0.02) in $Ni_{45}(Co_{1-x}Fe_x)_5Mn_{36.6}In_{13.4}$ can cause a big shift (8 K) of M_s from 279 K to 287 K [13]. In our previous work, $Ni_{40}Co_{10}Mn_{41}Sn_9$ undergoes martensitic transformation at about 410 K far above RT [14].

For ideal Ericsson cycle based magnetic refrigeration, magnetocaloric materials should possess a constant magnetic entropy change (ΔS_M) over a wide working temperature range [15]. Considering that the working temperature range is usually estimated as the full-width at half-maximum (δT_{FWHM}) of the thermal dependence of the magnetic entropy change curve $\Delta S_M(T)$, this means the magnitude of δT_{FWHM} should be large. However, for most Ni-Mn-Z Heusler alloys fabricated by conventional melting methods, such as induction or arc melting and melt spinning, the narrow temperature range of the first-order structural transition limits the working

temperature range, irrespective of the high value of ΔS_M. Therefore, how to extend the working temperature range has become an important and interesting subject for the investigation of Ni-Mn-Z magnetic refrigeration materials. A composite material [16, 17] showing two or more sucessive magnetic phase transitions is, from the practical and experimental point of view, a promising approach to this problem. It has been transferred to our recent work on $Ni_{40.6}Co_{8.5}Mn_{40.9}Sn_{10}$ unidirectional crystal grown by the Bridgman-Stockbarger method [18]. A wide δT_{FWHM} of 23 K has been realized resulting from the step-like martensitic transformation due to the chemical segregations typically occurred in the growth of unidirectional crystal [19] or single crystal [20, 21]. As a typical Ni-Mn-Z Heusler alloy, we also expect to widen the working temperature range in Ni-Co-Mn-In by applying this method. In this study, we prepared a $Ni_{42}Co_8Mn_{38}In_{12}$ directionally solidified rod using the Bridgman-Stockbarger method. It is shown that such a sample possesses a considerably wide δT_{FWHM} from 272 to 321 K under a magnetic field change of 5 T. Consequently, this alloy shows a large refrigerant capacity (*RC*) of 334 J kg^{-1} K^{-1} in spite that it has just a small value of ΔS_M (6.8 J kg^{-1} K^{-1}).

II. EXPERIMENTAL PROCEDURE

A directionally solidified rod with diameter 6 mm with nominal composition $Ni_{42}Co_8Mn_{38}In_{12}$ was grown by the Bridgman-Stockbarger technique using a Ni-Mn-Ga monocrystalline seed with [001] parallel to the growth direction. In spite of the seed crystal, grains nucleated resulting in a directionally solidified polycrystalline rod. The details of fabrication process are similar to Refs. [18, 21]. A 4.0 mm long section was cut from the rod near the seed end where the contents of Co and In varied strongly. The side far from the seed end was polished and used for structure and microstructure study. From this section, we cut a sample with the approximate dimensions 0.8×0.8×4.0 mm^3 for DSC and magnetic measurements. The location of the studied sample is schematically shown in Figure 1. The microstructure was

examined perpendicular to the growth direction using an OLYMPUS optical microscope and a LEO model 1430VP scanning electron microscope equipped with an energy dispersive X-ray spectroscopy (EDS) for measuring the chemical composition. The SEM image was taken in backscattering emission mode. XRD analysis was performed at room temperature using copper K_α radiation. The DSC measurements were performed in a TA INSTRUMENTS model Q200 under a high purity Ar flow at a heating/cooling rate of 10 K min^{-1}. Magnetization studies were carried out using the by vibrating sample magnetometry option of a Quantum Design PPMS® EverCool® -9T platform. The major length was parallel to the axial direction of the ingot, i.e. parallel to the direction of solidification. The magnetic field $\mu_o H$ was applied along the major length of this parallelepiped shaped sample to minimize the demagnetizing field effect. Owing to the strong effect of the magnetic field on the MST to AST phase transition, a fixed thermal protocol was followed prior to measure each isothermal magnetization each $M(\mu_o H)$ curve throughout MST → AST transition [22]: at zero magnetic field the sample is heated to 400 K to stabilize austenite, cooled to 100 K to completely form martensite, and then heated again in no-overshot mode to the selected measuring temperature T_{meas}. This procedure ensures that prior to apply the magnetic field the sample shows the phase constitution that correspond to the thermally induced structural transition.

III. EXPERIMENTAL RESULTS AND DISCUSSION

Fig. 1 shows the composition profiles for all the four alloy elements determined from EDS along the growth direction; the error in the determinations is estimated as ± 0.5 at. %. The first measurement was taken just after the Ni-Mn-Ga seed and henceforward every 2 mm. The approximate position of the specimen studied is about 1 mm from the seed, as indicated by the grey rectangle in the graph. The component concentration varies monotonically over the length as the distance from the seed increases, confirming the existence of chemical segregation which is

normal for crystals obtained using Bridgman method due to the intrinsic solutal partition during solidification [18, 20, 21]. For the studied sample, the contents of Ni and Mn changed slightly, while that of Co and In showed great changes, i.e., Co increased and In decreased remarkably along the growth direction. Compared with $Ni_{40.6}Co_{8.5}Mn_{40.9}Sn_{10}$ (without second phase) reported in Ref. [18], the present sample showed a stronger chemical segregation.

Fig. 2(a) and (b) are an XRD pattern and optical image taken at room temperature (293 K) from the cross section of the rod-shaped sample. Some characteristic peaks are missing, which may be due to the fact that the present sample was directionally solidified and may have a strong texture [23-25]. In spite of this, as evidenced by the optical observations in Fig. 2 (b), the XRD pattern can be indexed as a mixture of $L2_1$ austenite phase and martensite phase, denoted as A and M in the picture, respectively. For the martensite**,** the tetragonal structure is usually found for Ni-Mn based alloys with a low content of Sn or In [26, 27]. For example, Krenke et al. found with the decrease of Sn content in $Ni_{0.50}Mn_{0.50-x}Sn_x$, the crystal structure changed in the following sequence, $L2_1$ → orthorhombic → monoclinic → tetragonal [26]. Similar finding was also reported in $Ni_{50}Mn_{34}In_{16-x}Ga_x$ [27]. As the content of In for the present sample is less than 10 % as indicated in Fig. 1, the present martensite is believed to have a tetragonal structure. The lattice parameters were determined as follows: for austenite phase, a = 0.6086 nm, and for martensite phase, $a = b = 0.7853$ nm, $c = 0.6834$ nm, and $c/a = 0.87$. Except for the (202) main peak, more minor diffraction peaks occur for the present sample suggesting that it has a polycrystalline microstructure with a specific orientation. The optical micrograph shown in Fig. 2 (b) also reveals a polycrystalline microstructure. A few coarse grains can be clearly seen. There exist definite surface relief effects associated with martensite within several grains. This is in good agreement with the XRD result. Optical observation as shown in the inset of Fig. 2(b) is performed on a local area indicated by the square. The martensite is characterized by lath-like

morphology, coexisting with the austenite with grey color. Besides, some second phase particles precipitate within the grains or along the grain boundaries.

Fig. 2(c) shows a back-scattered electron (BSE) image. Many dark particles with various shape and size are observed, which appear as a second phase with a composition $Ni_{39.5}Co_{18.5}Mn_{41}In_{1.0}$. In comparison with the matrix ($Ni_{43.1}Co_{6.9}Mn_{39.1}In_{10.9}$), this second phase is richer in Co while poorer in In. Note that second phase particles are unevenly distributed within the matrix, which enhances the degree of chemical inhomogeneity. In addition, since the second phase does not participate in the magnetostructural transition, it is believed that it negatively influences magnetic field induced reverse transformation and weakens the MCE. This has been confirmed in $Ni_{46}Mn_{35}In_{14}Co_5$ ribbons, in which Co-rich γ as a second phase precipitates after high temperature annealing [3]. The value of ΔS_M is remarkably reduced by about 9.4 J kg^{-1} K^{-1} due to the formation of γ phase [3].

Fig. 3(a) shows the cooling/heating DSC curves. Between 275 and 350 K, a broad martensitic forward/reverse transformation was observed. Note that it is smooth and macroscopically different from the step-like martensitic transformation we recently reported in $Ni_{40.6}Co_{8.5}Mn_{40.9}Sn_{10}$ alloy [18]. However, the nature of both of them is ascribed to the chemical segregation along the growth direction during crystal growth with the Bridgman-Stockbarger method. To precisely detect the phase transition temperatures, the low-field (5 mT) magnetization as a function of temperature, $M(T)$, curve in heating from zero-field-cooled (ZFC) and cooling in magnetic field (FC) modes between 10 and 400 K was performed, a part of which is displayed in Fig. 3(b). The martensitic transformation start and finish temperatures, M_s and M_f, as well as the reverse transformation start and finish temperatures, A_s and A_f are determined by a conventional tangent extrapolation method. Under 5 mT field, M_s, M_f, A_s and A_f are 307, 263, 304, and 346 K, respectively. Room temperature (293 K), at which the optical image is taken, is between the M_s

and M_f. It means that the sample partially transforms to the martensite at room temperature and a large fraction of austenite remains, which results in the coexistence of martensite and austenite for the matrix as shown in Fig. 2 (a) and (b).

Fig. 3(c) shows the comparison between low-field (5 mT) and high-field (5 T) $M(T)$ curves heating in ZFC and cooling in FC modes between 100 and 400 K. Under a high magnetic field of 5 T, the magnetization for FC (25 A m^2 kg^{-1}) is higher than that for ZFC (10 A m^2 kg^{-1}) below about 195 K, the finish temperature of martensitic transformation (M_f) determined by the tangent method. That is, a splitting between the ZFC and FC pathways of the $M(T)$ curves occurs. For a complete martensitic transformation, the transition from high temperature austenite (ferromagnetic) to low temperature martensite (paramagnetic) decreases the magnetization value till that the single martensite possesses. That is, well below M_f, the overlap of FC and ZFC pathways should appear, as shown in 5 mT $M(T)$ curve. Consequently, under 5 T field, the splitting between the ZFC and FC pathways means martensitic transformation is interrupted at a certain temperature (195 K here) during FC and does not proceed with further cooling. Such a magnetic field-induced phenomenon is called kinetic arrest (KA) of martensitic transformation [28] and is frequently observed in Ni-Co-Mn-Z alloys which results in a metastable magnetic glass state [28-32]. By applying 5 T field, those transformation temperatures are dropped to 295, 195, 243, and 324 K by reductions of 12, 68, 61, and 22 K, respectively. Thus, the rates of temperature change of relative to the field, $\Delta T/\mu_o \Delta H$, for A_s and A_f are 12.2 and 4.4 K/T, respectively. If room temperature (293 K) is selected as a measuring temperature, the minimum field needed to achieve a complete reversible transformation (H_{min}) at room temperature is determined to be 12 T using the equation: $H_{min} = (A_{f,0} - A_{f,H})/(\Delta T/\mu_o \Delta H)$. Here, $A_{f,0}$ and $A_{f,H}$ represent the magnitude of A_f under zero and the applied fields. They are 346 and 293 K, respectively. The application of 2 T field shift A_s and A_f to be 280 and 337 K, respectively.

According to the $M(T)$ curves, the percentage of reverse martensitic transformation can be determined by the temperature interval between the measuring temperature and A_s (T_{mea} - A_s) divided by the whole transformation interval (A_f - A_s) under an application of magnetic field. It is nearly 42.4 % under 2 T field. Notice that the magnetic field has a strong and various influence on the shift of transformation temperatures. The decreases of A_s and M_f are much larger than for M_s and A_f. Therefore, the magnetic field significantly widen the transformation interval for the reverse transformation, ΔT_R, since it increases from 42 K (5 mT) to 81 K (5 T). Such a large ΔT_R helps to achieve a greater *RC* value [16]. In addition, the magnetization difference between the austenite and martensite, $\Delta M_{A\text{-}M}$ is about 86 A m^2 kg^{-1} under 5 T field, which is considerable and is one of the causes leading to large transformation temperature change induced by the magnetic field change according to the Clausius-Clapeyron relation in the magnetic phase diagram [33]. Such a high $\Delta M_{A\text{-}M}$ also provides more driving force to induce the structural transition by a relatively low magnetic field [34, 35].

For assessing the potential for cyclic use, the magnetocaloric reversible region under 5 T field is determined according to the rule proposed by Stern-Taulats et al. [36]. Under a given magnetic field, in the vicinity of a magnetostructural first-order transition, the magnetocaloric reversible region extends from the start temperature of the forward transition at zero field to the start temperature of the reverse transition under applied field [36]. For the present paper, the start temperature of the forward transition at zero field is 307 K, and the start temperature of the reverse transition under an applied field of 5 T is 243 K. Therefore, the magnetocaloric reversible region for the present sample under 5 T field is between 243 K and 307 K. Further investigation should be done to achieve a comprehensive understanding on the reversibility of magnetocaloric effect for the sample with a broad transformation interval.

Fig. 4(a) shows the isothermal magnetization versus magnetic field, $M(\mu_o H)$ curves around the reverse martensitic transformation. Between 250 K and 323.5 K, the metamagnetic-like behaviour occurs, i.e., with increasing magnetic field, the magnetization initially saturates quickly by applying a low $\mu_o H$ followed by a distinct increase of the slope dM/dH above a specific critical field. This is due to the field induced transition from low magnetization martensite to a higher magnetization austenite. In previously reported Ni-(Co)-Mn-In Heusler alloys, such a temperature interval (ΔT_M) within which magnetic field induced reverse transformation takes place usually does not exceed 40 K [13, 37, 38]. For example, ΔT_M for $Ni_{50}Mn_{34}In_{16}$ is around 40 K [37], and about 20 K for $Ni_{45}Co_5Mn_{36.6}In_{13.4}$ [13]. Even for $Ni_{40}Co_{10}Mn_{40}Sn_{10}$, which exhibits the largest RC (~ 426 J kg^{-1} for 5 T) among the Ni-Mn-based Heusler alloys, ΔT_M is just 40 K [6]. To our knowledge, ΔT_M of 73.5 K for the present sample is the widest for all the Ni-Mn-Z Heusler alloys. It may be due to a large ΔT_R (81 K) especially under 5 T field and a high $\Delta M_{A\text{-}M}$ (86 A m^2 kg^{-1}). Above 325 K, it just shows a simple ferromagnetic behavior with increasing field.

Arrott plots, as shown in Fig. 4(b), are obtained by plotting the values of $M(\mu_o H)$ and $\mu_o H$ as a function of M^2 versus $\mu_o H/M$ [39, 40]. As confirmed in Refs. [41, 42], the phase transition order may be judged by the shape of low-field Arrott plots near phase transition temperature. That is, first-order transition (FOT) is characterized by S-shape Arrott plots while second-order transition (SOT) displays linear behaviours in the plots. From Fig. 4(b), the phase transition is of first-order type as the plots at temperature ranging from 300 to 334 K when $\mu_o H/M$ lower than 0.05 T kg A^{-1} m^{-2} exhibit S shape.

We calculate the ΔS_M using the Maxwell relation (i.e., $\Delta S_M(T,\mu_0 H) = \mu_0 \int_0^{\mu_0 H} \left[\frac{\partial M(T,\mu_0 H')}{\partial T}\right]_{\mu_0 H'} dH'$) and plot its dependence on the temperature and magnetic field change in Fig. 5(a). It can be seen that the maximum entropy change ΔS_M^{peak}

increases with field change as shown in the inset of Fig. 5(b). For $\mu_o\Delta H$ = 5 T, the ΔS_M^{peak} reaches 6.8 J kg^{-1} K^{-1} which is a relatively small magnetic entropy change among Ni-Mn-Z alloys but it is inversely proportional to δT_{FWHM}. The entropy change shows a "hump-like" behaviour as a function of temperature instead of a spike-like $\Delta S_M(T)$ curve in other Ni-Mn-Z alloys [2, 4, 7, 10, 43] suggesting a broader working temperature range for this directionally solidified sample. Here, we use δT_{FWHM}, the full-width at half-maximum of the $\Delta S_M(T)$ curve, i.e., the difference between T_{hot} and T_{cold}, to evaluate the working temperature range. Both T_{hot} and T_{cold} shift to low temperatures but with various changing rate upon increasing magnetic field. T_{cold} decreases more quickly than T_{hot} indicating that δT_{FWHM} is broadened upon the application of magnetic field. The general tendency of the changes of T_{hot} and T_{cold} is indicated by a blue and yellow arrow, respectively in Fig. 5(b) and the detailed values of δT_{FWHM}, T_{hot} and T_{cold} are illustrated in Table I. Under 5 T field, δT_{FWHM} reaches up to 49 K. T_{hot} = 321 K and T_{cold} = 272 K. This may yield a high *RC* near room temperature even though the present ΔS_M is relatively small. The values of *RC* under several selected field are calculated using the relation $RC = |\Delta S_M^{peak}| \times \delta T_{FWHM}$ [15] and listed in Table I. For $\mu_o\Delta H$ = 5 T, the sample exhibits a considerably great *RC* (334 J kg^{-1}).

For comparison, the *RC* values for the present sample, some studied Ni-Mn-Z magnetocaloric alloys, and $Gd_5Ge_2Si_2$ (the most promising room temperature magnetic cooling material) are schematically illustrated in Fig. 6. The length of the bar where *RC* value located represents the width of working temperature interval (i.e., δT_{FWHM}). The present sample possesses a very large *RC* value comparable to $Gd_5Ge_2Si_2$ and greater than most Ni-Mn-Z alloys. Most importantly, this sample exhibits the widest δT_{FWHM} near room temperature among the reported Ni-Mn-Z magnetic refrigeration materials reported so far. For $Ni_{40.6}Co_{8.5}Mn_{40.9}Sn_{10}$ alloy in our previous study, a wide δT_{FWHM} of 23 K was also reported, which may be ascribed to the chemical segregation along the growth direction during single crystal growth with the Bridgman-

Stockbarger method [18]. The same reason plus the formation of second phase can account for such a broad δT_{FWHM} in our present $Ni_{42}Co_8Mn_{38}In_{12}$ alloy. These two results suggest that, to widen δT_{FWHM} in Ni-Mn-Z alloys, Bridgman-Stockbarger technique is a good option. The present broad working temperature range occurs within the first 5 mm close to the seed end where the contents of Co and In varied strongly. Thus, in order to effectively used Bridgman-Stockbarger technique to prepare a sample with a strong chemical segregation, more investigations on the correlationship between the composition profiles and processing conditions should be carried out. For example, it is feasible to shorten the duration of homogenizing treatment after the growth of directionally solidified rod.

For Ni-Mn-Z magnetic refrigeration materials, the hysteresis losses originated in the field-induced reverse martensitic transformation is inevitable and should be deducted from the value of *RC* to obtain an effective one, RC_{eff}. They were estimated from the set of isothermal magnetization curves measured on increasing and decreasing the field as shown in Fig. 7(a) and (b). The maximum magnetic field of 2 T and 5 T was applied, respectively. For these two applied field, the hysteresis loss, *HL*, dependence on the temperature is displayed in Fig. 7(c). Obviously, *HL* was remarkably increased with increasing the applied field. The average hysteresis loss, $\langle HL \rangle$ was about -9.6 and -55 J kg^{-1} for 2 T and 5 T field, respectively. The magnitude of $\langle HL \rangle$ at $\mu_o \Delta H$ = 2 T is much smaller than that (-19 J kg^{-1}) in $Ni_{40.6}Co_{8.5}Mn_{40.9}Sn_{10}$ unidirectional crystal sample [18]. Thus, by substracting the $\langle HL \rangle$ from the corresponding *RC* value at 2 T (i.e., 127 J kg^{-1}), RC_{eff} (2 T) is found to be 117.4 J kg^{-1}. Similarly, for 5 T field change, RC_{eff} is 279 J kg^{-1}. RC_{eff} under either of these two fields is much higher than $Ni_{49}Mn_{39}Sn_{12}$ (58 J kg^{-1}) [19] and $Mn_{50}Ni_{40}In_{10}$ (76.7 J kg^{-1}) [44] crystals grown using a modified high-pressure optical zone-melting technique. It should be noted that, RC_{eff} for $Ni_{49}Mn_{39}Sn_{12}$ and $Mn_{50}Ni_{40}In_{10}$ crystals are

caused only by martensitic transformation as the present $Ni_{40.6}Co_{8.5}Mn_{40.9}Sn_{10}$ alloy, while at a higher field of $\mu_o\Delta H$ = 3 T.

IV. CONCLUSIONS

A directionally solidified $Ni_{42}Co_8Mn_{38}In_{12}$ rod was grown using the Bridgman-Stockbarger method. Its initial part exhibits a first-order phase transformation around room temperature with a considerably wide transformation interval which progressively increases by application of the magnetic field. Thus, a large value of refrigerant capacity (334 J kg^{-1}) along with a broad working temperature range from 272 to 321 K is achieved. More importantly, the average hysteresis loss maintains a low value of -9.6 J kg^{-1}. Chemical heterogeneity introduced by chemical segregation through the Bridgman-Stockbarger method and enhanced by decomposition via precipitation extends the working temperature range for Ni-Mn-Z magnetic refrigeration materials.

ACKNOWLEDGEMENTS

The National Natural Science Foundation of China (51101040), the Fundamental Research Funds for the Central Universities (HEUCF171007), and the State Scholarship Fund of China, supported this work. PM acknowledges financial support through the National Science Foundation through grant No DMR-1207192. J.L. Sánchez Llamazares acknowledges financial support received from Laboratorio Nacional de Investigaciones en Nanociencias y Nanotecnología (LINAN, IPICYT).

REFERENCES

[1] T. Krenke, E. Duman, M. Acet, E.F. Wassermann, X. Moya, L. Mañosa, A. Planes, Nat. Mater. 4 (2005) 450-454.

[2] A.K. Nayak, K.G. Suresh, A.K. Nigam, J. Phys. D: Appl. Phys. 42 (2008) 035009.

[3] J. Liu, T.G. Woodcock, N. Scheerbaum, O. Gutfleisch, Acta Mater. 57 (2009) 4911-4920.

[4] Z.D. Han, D.H. Wang, B. Qian, J.F. Feng, X.F. Jiang, Y.W. Du, Jpn. J. Appl. Phys. 49 (2010) 010211.

[5] J. Liu, T. Gottschall, K.P. Skokov, J.D. Moore, O. Gutfleisch, Nat. Mater. 11 (2012) 620-626.

[6] L. Huang, D.Y. Cong, H.L. Suo, Y.D. Wang, Appl. Phys. Lett. 104 (2014) 132407.

[7] S. Aksoy, T. Krenke, M. Acet, E.F. Wassermann, X. Moya, L. Mañosa, A. Planes, Appl. Phys. Lett. 91 (2007) 241916.

[8] M. Khan, N. Ali, S. Stadler, J. Appl. Phys. 101 (2007) 053919.

[9] Z.D. Han, D.H. Wang, C.L. Zhang, H.C. Xuan, B.X. Gu, Y.W. Du, Appl. Phys. Lett. 90 (2007) 042507.

[10] T. Krenke, E. Duman, M. Acet, X. Moya, L. Mañosa, A. Planes, J. Appl. Phys. 102 (2007) 033903.

[11] H.S. Liu, C.L. Zhang, Z.D. Han, H.C. Xuan, D.H. Wang, Y.W. Du, J. Alloys Compd. 467 (2009) 27-30.

[12] D.Y. Cong, S. Roth, M. Pötschke, C. Hürrich, L. Schultz, Appl. Phys. Lett. 97 (2010) 021908.

[13] L. Chen, F.X. Hu, J. Wang, L.F. Bao, J.R. Sun, B.G. Shen, J.H. Yin, L.Q. Pan, Appl. Phys. Lett. 101 (2012) 012401.

[14] F. Chen, Y.X. Tong, B. Tian, L. Li, Y.F. Zheng, Y. Liu, J. Magn. Magn. Mater. 347 (2013) 72-74.

[15] A.M. Tishin, Y.I. Spichkin, The magnetocaloric effect and its applications, Institute of Physics Publishing, Bristol, 2003.

[16] A. Chaturvedi, S. Stefanoski, M.H. Phan, G.S. Nolas, H. Srikanth, Appl. Phys. Lett. 99 (2011) 162513.

[17] H.C. Tian, X.C. Zhong, Z.W. Liu, Z.G. Zheng, J.X. Min, Materials Letters 138 (2015) 64-66.

[18] F.Chen, Y. X.Tong, L.Li, J. L.Sánchez Llamazares, C. F.Sánchez-Valdés, P.Müllner, J. Alloys Compd. 691 (2017) 269-274.

[19] J. Ren, H. Li, J. Yu, S. Feng, Q. Zhai, J. Fu, Z. Luo, H. Zheng, J. Alloys Compd. 634 (2015) 65-69.

[20] D.L. Schlagel, Y.L. Wu, W. Zhang, T.A. Lograsso, J. Alloys Compd. 312 (2000) 77-85.

[21] D. Kellis, A. Smith, K. Ullakko, P. Müllner, J. Cryst. Growth 359 (2012) 64-68.

[22] A. Quintana-Nedelcos, J.L. Sánchez Llamazares, C.F. Sánchez-Valdés, P. Álvarez Alonso, P. Gorria, P. Shamba, N.A. Morley, J. Alloys Compd. 694 (2017) 1189-1195.

[23] M. Pötschke, U. Gaitzsch, S. Roth, B. Rellinghaus, L. Schultz, J. Magn. Magn. Mater. 316 (2007) 383-385.

[24] P. Zheng, N.J. Kucza, Z. Wang, P. Müllner, D.C. Dunand, Acta Mater. 86 (2015) 95-101.

[25] G. Uwe, C. Robert, W. Linda, B. Andrea, S. Werner, O. Carl‐Georg, B. Heinz‐Günter, L. Thomas, N. Iñaki, P. Martin, Advanced Engineering Materials 14 (2012) 636-652.

[26] T. Krenke, M. Acet, E.F. Wassermann, X. Moya, L. Mañosa, A. Planes, Phys. Rev. V 72 (2005).

[27] Z.H. Liu, G.T. Li, Z.G. Wu, X.Q. Ma, Y. Liu, G.H. Wu, J. Alloys Compd. 535 (2012) 120-123.

[28] R.Y. Umetsu, K. Ito, W. Ito, K. Koyama, T. Kanomata, K. Ishida, R. Kainuma, J. Alloys Compd. 509 (2011) 1389-1393.
[29] W. Ito, R.Y. Umetsu, R. Kainuma, T. Kakeshita, K. Ishida, Scr. Mater. 63 (2010) 73-76.
[30] Y.H. Lee, M. Todai, T. Okuyama, T. Fukuda, T. Kakeshita, R. Kainuma, Scr. Mater. 64 (2011) 927-930.
[31] K.N. Ajaya, K.G. Suresh, A.K. Nigam, J. Phys.: Cond. Matter 23 (2011) 416004.
[32] L. Archana, A. Banerjee, P. Chaddah, X. Chen, R.V. Ramanujan, J. Phys.: Cond. Matter 24 (2012) 386004.
[33] R. Kainuma, Y. Imano, W. Ito, Y. Sutou, H. Morito, S. Okamoto, O. Kitakami, K. Oikawa, A. Fujita, T. Kanomata, K. Ishida, Nature 439 (2006) 957-960.
[34] S.Y. Yu, Z.X. Cao, L. Ma, G.D. Liu, J.L. Chen, G.H. Wu, B. Zhang, X.X. Zhang, Appl. Phys. Lett. 91 (2007) 102507.
[35] W. Ito, X. Xu, R.Y. Umetsu, T. Kanomata, K. Ishida, R. Kainuma, Appl. Phys. Lett. 97 (2010) 242512.
[36] E. Stern-Taulats, P.O. Castillo-Villa, L. Mañosa, C. Frontera, S. Pramanick, S. Majumdar, A. Planes, J. Appl. Phys. 115 (2014) 173907.
[37] V.K. Sharma, M.K. Chattopadhyay, S.B. Roy, J. Phys. D: Appl. Phys. 40 (2007) 1869-1873.
[38] T. Krenke, E. Duman, M. Acet, E. Wassermann, X. Moya, L. Mañosa, A. Planes, E. Suard, B. Ouladdiaf, Phys. Rev. B 75 (2007).
[39] A. Arrott, Physical Review 108 (1957) 1394.
[40] K.U. Neumann, K.R.A. Ziebeck, J. Magn. Magn. Mater. 140-144 (1995) 967-968.
[41] D.H. Wang, S.L. Tang, S.L. Huang, J.R. Zhang, Y.W. Du, J. Magn. Magn. Mater. 268 (2004) 70-74.
[42] Q.Y. Dong, J. Chen, J. Shen, J.R. Sun, B.G. Shen, J. Magn. Magn. Mater. 324 (2012) 2676-2678.
[43] T.L. Phan, P. Zhang, N.H. Dan, N.H. Yen, P.T. Thanh, T.D. Thanh, M.H. Phan, S.C. Yu, Appl. Phys. Lett. 101 (2012) 212403.
[44] J. Ren, H. Li, S. Feng, Q. Zhai, J. Fu, Z. Luo, H. Zheng, Intermetallics 65 (2015) 10-14.
[45] J. Du, Q. Zheng, W.J. Ren, W.J. Feng, X.G. Liu, Z.D. Zhang, J. Phys. D: Appl. Phys. 40 (2007) 5523-5526.
[46] V.K. Sharma, M.K. Chattopadhyay, L.S. Sharath Chandra, S.B. Roy, J. Phys. D: Appl. Phys. 44 (2011) 145002.
[47] S. Fabbrici, J. Kamarad, Z. Arnold, F. Casoli, A. Paoluzi, F. Bolzoni, R. Cabassi, M. Solzi, G. Porcari, C. Pernechele, Acta Mater. 59 (2011) 412-419.
[48] P.O. Castillo-Villa, L.s. Mañosa, A. Planes, D.E. Soto-Parra, J.L. Sánchez-Llamazares, H. Flores-Zúñiga, C. Frontera, J. Appl. Phys. 113 (2013) 053506.
[49] Z. Li, Y. Zhang, C.F. Sánchez-Valdés, J.L. Sánchez Llamazares, C. Esling, X. Zhao, L. Zuo, Appl. Phys. Lett. 104 (2014) 044101.
[50] R.D. Shull, V. Provenzano, A.J. Shapiro, A. Fu, M.W. Lufaso, J. Karapetrova, G. Kletetschka, V. Mikula, J. Appl. Phys. 99 (2006) 08K908.
[51] I. Babita, S.I. Patil, S. Ram, J. Phys. D: Appl. Phys. 43 (2010) 205002.
[52] D. Bourgault, J. Tillier, P. Courtois, D. Maillard, X. Chaud, Appl. Phys. Lett. 96 (2010) 132501.

TABLE CAPTIONS

Table I. The magnitudes of ΔS_M^{peak}, RC, δT_{FWHM}, T_{hot} and T_{cold} for selected values of applied magnetic field.

FIGURE CAPTIONS

Fig. 1 Composition profiles determined by EDS along the growth direction for the directionally solidified rod. The grey rectangle shows the approximate location of the studied sample.

Fig. 2 (a) XRD trace and (b) optical image taken from the cross section of the directionally solidified rod at room temperature. The letters A and M in (a) represent the austenite and martensite phase, respectively. The inset in (b) is the surface morphology of the square area. (c) SEM image taken in backscattering emission mode showing the presence of second phase particles with a dark contrast. Chemical compositions of the matrix and second phase are also indicated.

Fig. 3 (a) Heating and cooling DSC curve. (b) Thermal dependence of magnetization, $M(T)$ curve measured in ZFC and FC regimens under a static magnetic field of 5 mT. (c) $M(T)$ curves measured in ZFC and FC regimens under static magnetic fields of 5 mT and 5 T.

Fig. 4 Isothermal magnetization curves (a) and Arrott plots (b) obtained in the temperature range of 250-334 K across the reverse martensitic transformation.

Fig. 5 (a) $\Delta S_M(T)$ curves determined each 0.5 T from 0.5 to 5 T. The vertical arrow indicates the field sequence of data collection. The red and blue dashed arrows roughly represent the dependence of T_{hot} and T_{cold} on the magnetic field change. (b) ΔS_M^{peak} and the temperatures T_{hot} and T_{cold} that define the δT_{FWHM} as a function of the magnetic field change.

Fig. 6 RC and working temperature range under a magnetic field change of 5 T for $Ni_{40}Co_{10}Mn_{40}Sn_{10}$ [6], $Ni_{45}Co_5Mn_{36.6}In_{13.4}$ [13], $Ni_{40.6}Co_{8.5}Mn_{40.9}Sn_{10}$ [18], $Ni_{50}Mn_{34}In_{16}$ [37], $Ni_{50}Mn_{37}Sn_{13}$ [43], $Ni_{50}Mn_{37}Sb_{13}$ [45], $Ni_{50}(Mn,2\%Cr)_{34}In_{16}$ [46], $Ni_{43}Co_7Mn_{31}Ga_{19}$ [47],

$Ni_{43}Mn_{40}Sn_{10}Cu_7$ [48], $Ni_{52}Mn_{26}Ga_{22}$ [49], and $Gd_5Ge_2Si_2$ (the most promising room temperature magnetic cooling material) [50]. The values of $Ni_{49}Mn_{37.4}Sn_{13.6}$ [51] are obtained for $\mu_o\Delta H$ = 2 T and $Ni_{45}Co_5Mn_{37.5}In_{12.5}$ [52] for $\mu_o\Delta H$ = 7 T, respectively. As indicated in the figure, the high temperature end and low temperature end of *RC* horizontal bar correspond to T_{hot} and T_{cold}, respectively. The red star represents the present sample, $Ni_{43.1}Co_{6.9}Mn_{39.1}In_{10.9}$.

Fig. 7 (a) and (b) Isothermal magnetization curves on increasing (field-up) and decreasing (field-down) the magnetic field up to $\mu_o\Delta H_{max}$ = 2 T and 5 T, respectively. (c) Hysteresis loss across the MST to AST transition up to $\mu_o\Delta H_{max}$ = 2 T and 5 T, respectively.

Table I The magnitudes of ΔS_M^{peak}, RC, δT_{FWHM}, T_{hot} and T_{cold} for selected values of applied magnetic field change.

$\mu_o \Delta H$ (T)	ΔS_M^{peak} (J K^{-1} kg^{-1})	RC (J kg^{-1})	δT_{FWHM} (K)	T_{hot} (K)	T_{cold} (K)
1.0	1.5	60	41	329	288
2.0	3.0	127	43	327	284
3.0	4.4	195	44	324	280
4.0	5.7	265	47	323	276
5.0	6.8	334	49	321	272

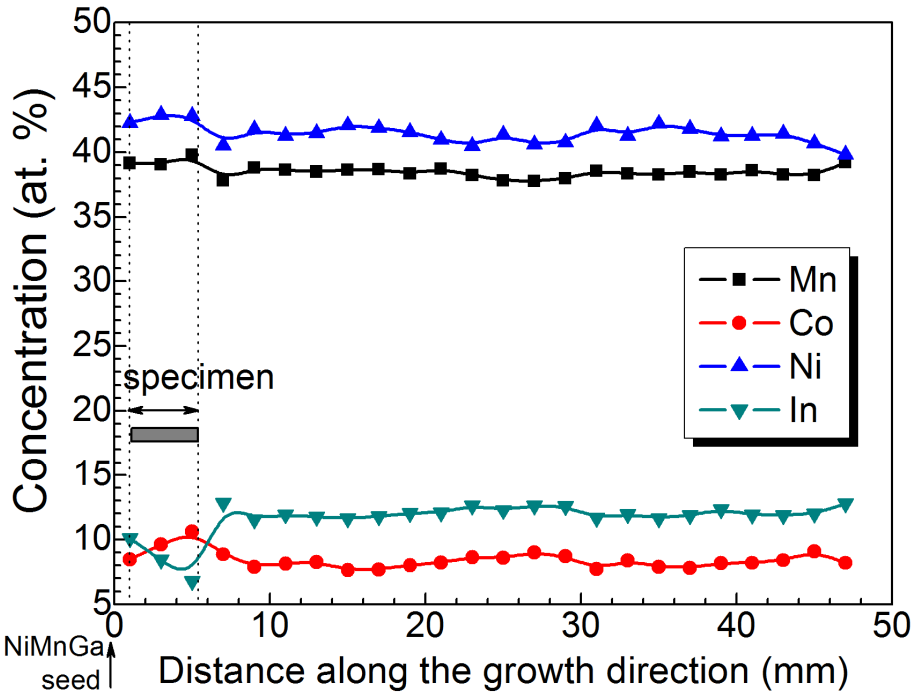

Fig. 1 Composition profiles determined by EDS along the growth direction for the directionally solidified rod. The grey rectangle shows the approximate location of the studied sample.

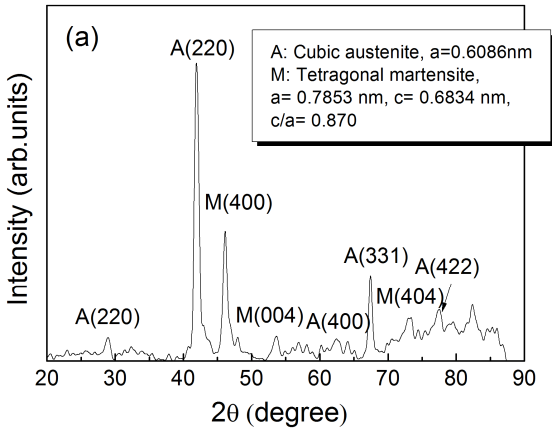

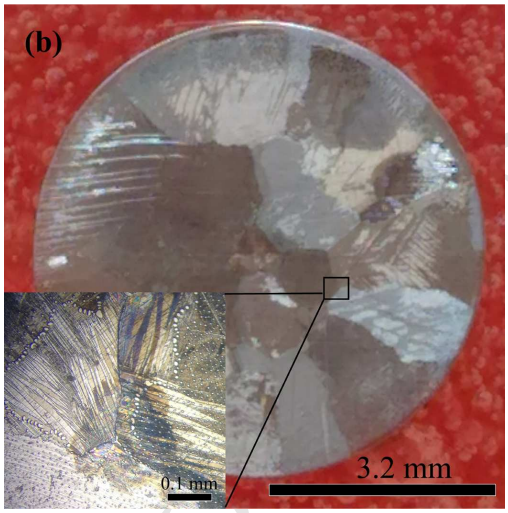

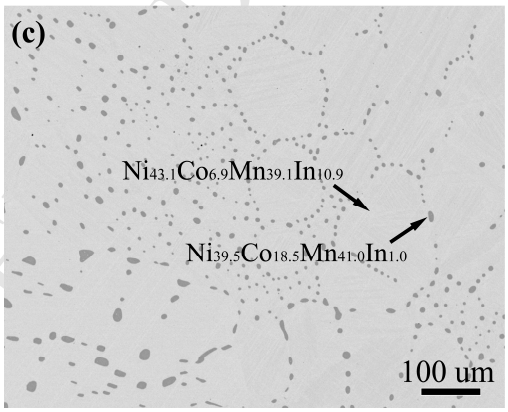

Fig. 2 (a) XRD trace and (b) optical image taken from the cross section of the directionally solidified rod at room temperature. The letters A and M in (a) represent the austenite and martensite phase, respectively. The inset in (b) is the surface morphology of the square area. (c) SEM image taken in backscattering emission mode showing the presence of second phase particles with a dark contrast. Chemical compositions of the matrix and second phase are also indicated.

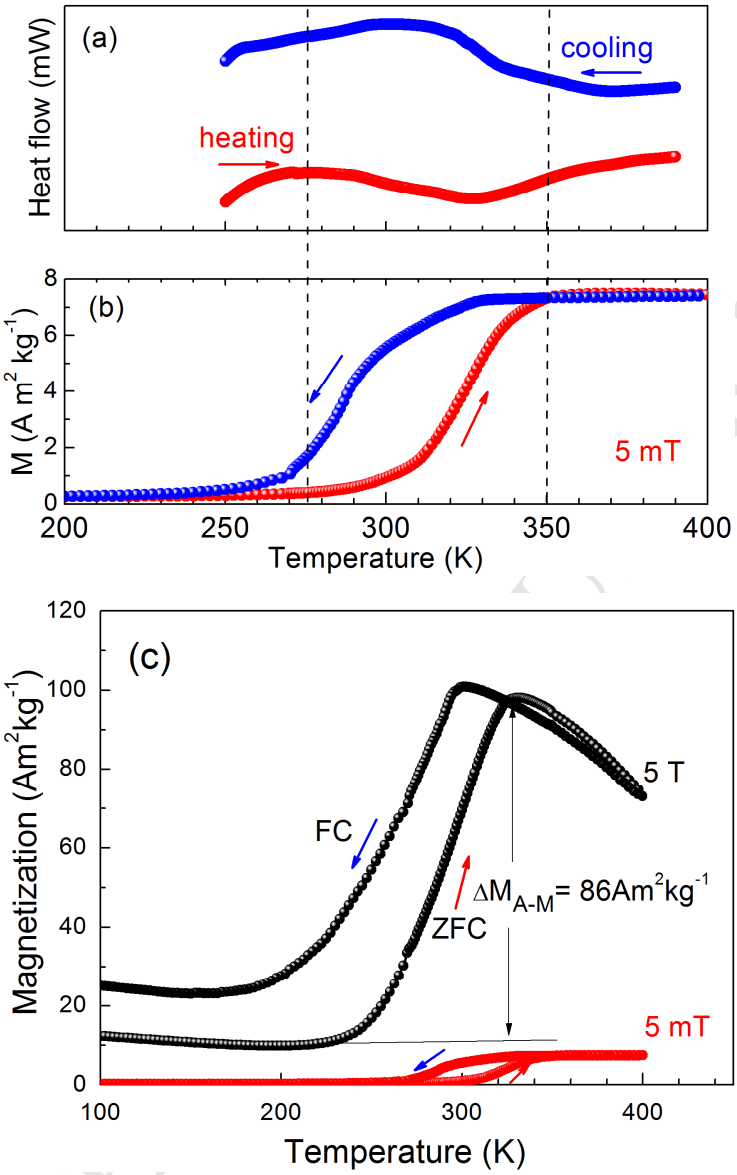

Fig. 3 (a) Heating and cooling DSC curve. (b) Thermal dependence of magnetization, $M(T)$ curve measured in ZFC and FC regimens under a static magnetic field of 5 mT. (c) $M(T)$ curves measured in ZFC and FC regimens under static magnetic fields of 5 mT and 5 T.

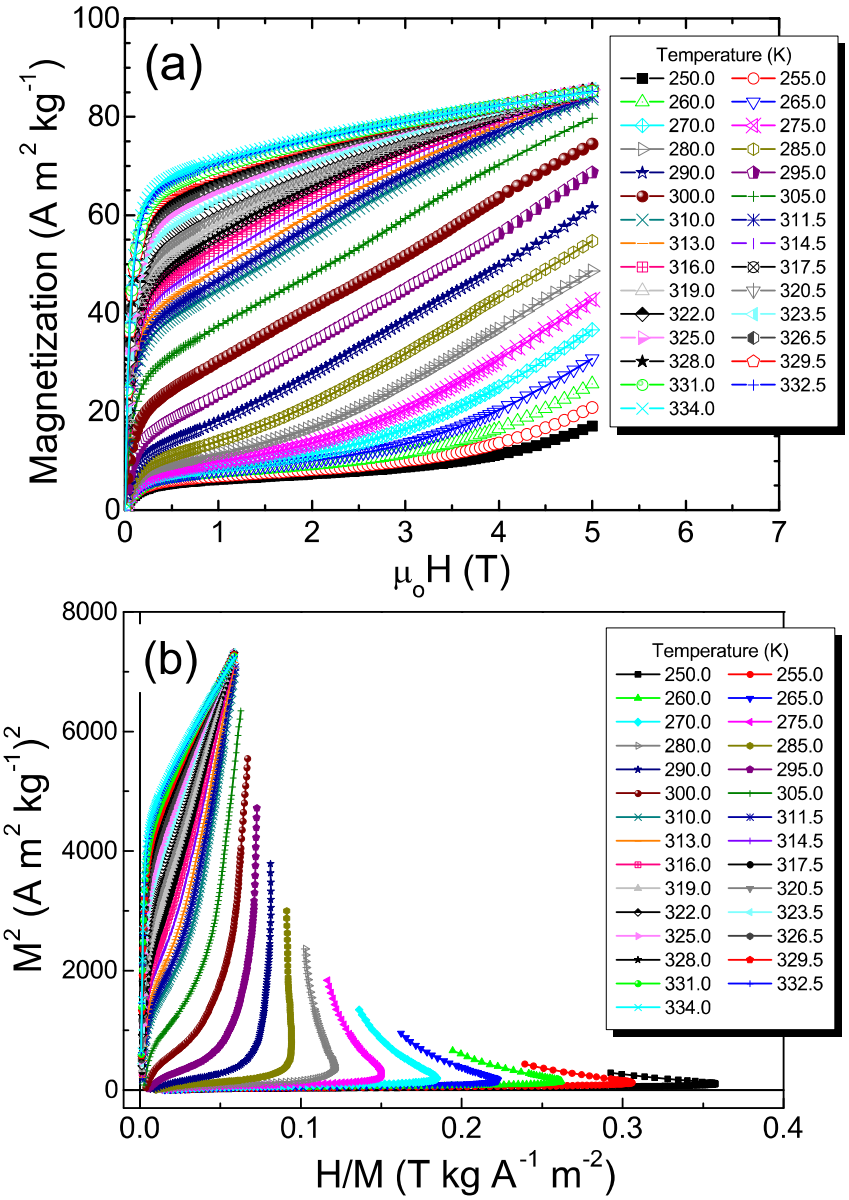

Fig. 4 Isothermal magnetization curves (a) and Arrott plots (b) obtained in the temperature range of 250-334 K across the reverse martensitic transformation.

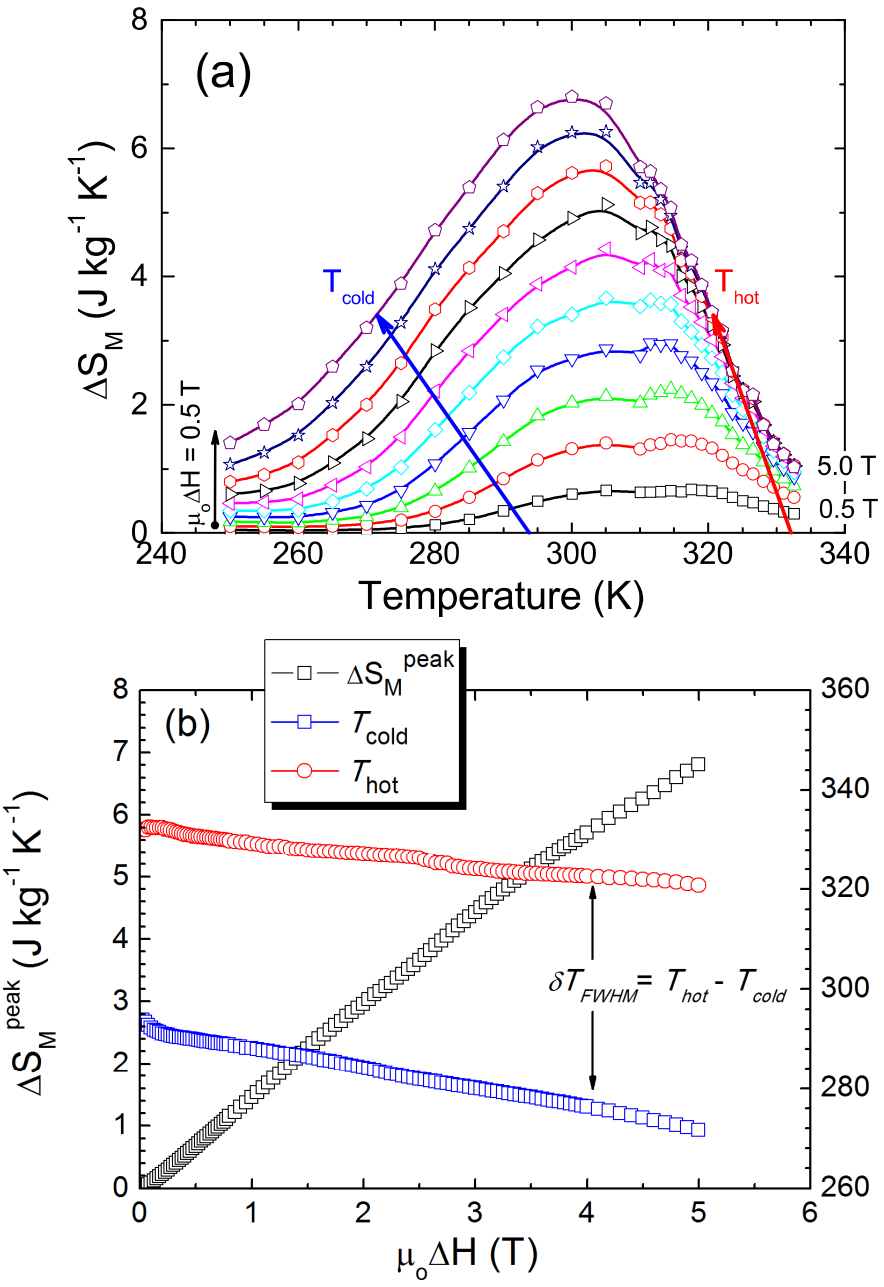

Fig. 5 (a) $\Delta S_M(T)$ curves determined each 0.5 T from 0.5 to 5 T. The vertical arrow indicates the field sequence of data collection. The red and blue dashed arrows roughly represent the dependence of T_{hot} and T_{cold} on the magnetic field change. (b) ΔS_M^{peak} and the temperatures T_{hot} and T_{cold} that define the δT_{FWHM} as a function of the magnetic field change.

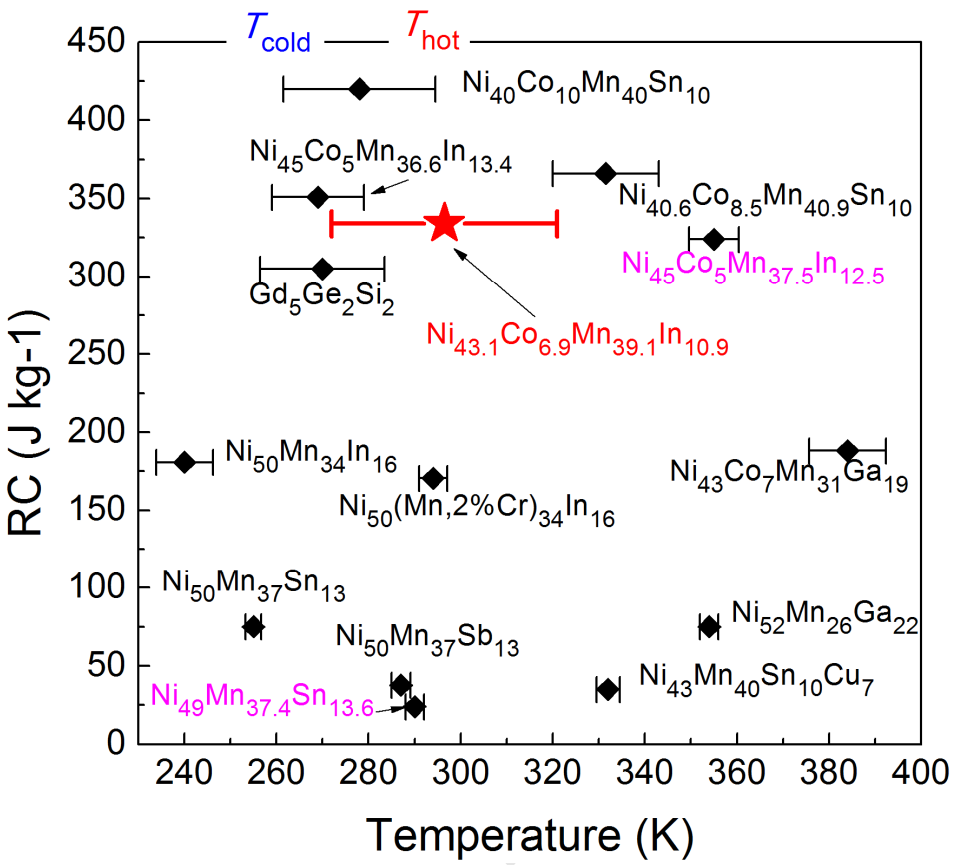

Fig. 6 *RC* and working temperature range under a magnetic field change of 5 T for $Ni_{40}Co_{10}Mn_{40}Sn_{10}$ [6], $Ni_{45}Co_5Mn_{36.6}In_{13.4}$ [13], $Ni_{50}Mn_{34}In_{16}$ [37], $Ni_{50}Mn_{37}Sn_{13}$ [43], $Ni_{50}Mn_{37}Sb_{13}$ [45], $Ni_{50}(Mn,2\%Cr)_{34}In_{16}$ [46], $Ni_{43}Co_7Mn_{31}Ga_{19}$ [47], $Ni_{43}Mn_{40}Sn_{10}Cu_7$ [48], $Ni_{52}Mn_{26}Ga_{22}$ [49], and $Gd_5Ge_2Si_2$ (the most promising room temperature magnetic cooling material) [50]. The values of $Ni_{49}Mn_{37.4}Sn_{13.6}$ [51] are obtained for μ_oH = 2 T and $Ni_{45}Co_5Mn_{37.5}In_{12.5}$ [52] for μ_oH = 7 T, respectively. As indicated in the figure, the high temperature end and low temperature end of *RC* horizontal bar correspond to T_{hot} and T_{cold}, respectively. The red star represents the present sample, $Ni_{43.1}Co_{6.9}Mn_{39.1}In_{10.9}$.

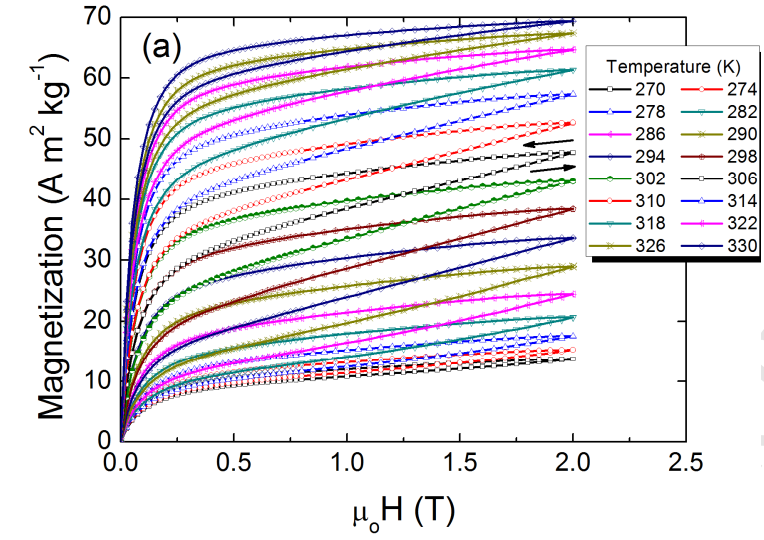

1

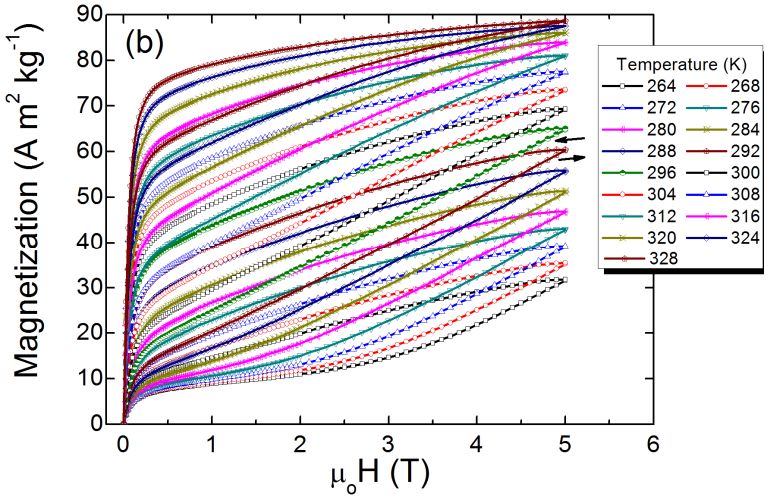

2

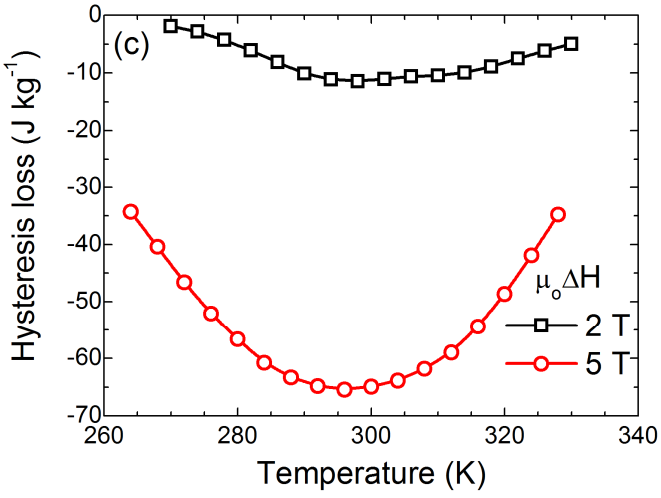

3

4 Fig. 7 (a) and (b) Isothermal magnetization curves on increasing (field-up) and decreasing (field-
5 down) the magnetic field up to $\mu_o\Delta H_{max}$ = 2 T and 5 T, respectively. (c) Hysteresis loss across the
6 MST to AST transition up to $\mu_o\Delta H_{max}$ = 2 T and 5 T, respectively.

Highlights

1. Chemical heterogeneity is enhanced by decomposition via precipitation.
2. The working temperature range is extended to 49 K.
3. A large value of refrigerant capacity (334 J kg^{-1}) is achieved.